Wang, Qingbo; Xu, Wenyang; Koppolu, Rajesh; van Bochove, Bas; Seppälä, Jukka; Hupa, Leena; Willför, Stefan; Xu, Chunlin; Wang, Xiaoju

Injectable thiol-ene hydrogel of galactoglucomannan and cellulose nanocrystals in delivery of therapeutic inorganic ions with embedded bioactive glass nanoparticles

Published in:
Carbohydrate Polymers

DOI:
10.1016/j.carbpol.2021.118780

Published: 15/01/2022

Document Version
Publisher's PDF, also known as Version of record

Carbohydrate Polymers 276 (2022) 118780

Contents lists available at ScienceDirect

Carbohydrate Polymers

journal homepage: www.elsevier.com/locate/carbpol

Injectable thiol-ene hydrogel of galactoglucomannan and cellulose nanocrystals in delivery of therapeutic inorganic ions with embedded bioactive glass nanoparticles

Qingbo Wang [a,1], Wenyang Xu [a,1], Rajesh Koppolu [a], Bas van Bochove [b], Jukka Seppälä [b], Leena Hupa [c], Stefan Willför [a], Chunlin Xu [a], Xiaoju Wang [a,d,*]

[a] Laboratory of Natural Materials Technology, Åbo Akademi University, Henrikinkatu 2, Turku FI-20500, Finland
[b] Polymer Technology, School of Chemical Engineering, Aalto University, Kemistintie 1D, Espoo FI-02150, Finland
[c] Laboratory of Molecular Science and Technology, Åbo Akademi University, Henrikinkatu 2, Turku FI-20500, Finland
[d] Pharmaceutical Sciences Laboratory, Faculty of Science and Engineering, Åbo Akademi University, Tykistökatu 6A, Turku FI-20520, Finland

ARTICLE INFO

Keywords:
Photo-crosslinkable injectable hydrogels
Thiol-ene chemistry
Thiolated cellulose nanocrystal
Galactoglucomannan methacrylate
Bioactive glass nanoparticles

ABSTRACT

We propose an injectable nanocomposite hydrogel that is photo-curable *via* light-induced thiol-ene addition between methacrylate modified *O*-acetyl-galactoglucomannan (GGMMA) and thiolated cellulose nanocrystal (CNC-SH). Compared to free-radical chain polymerization, the orthogonal step-growth of thiol-ene addition allows a less heterogeneous hydrogel network and more rapid crosslinking kinetics. CNC-SH reinforced the GGMMA hydrogel as both a nanofiller and a crosslinker to GGMMA resulting in an interpenetrating network *via* thiol-ene addition. Importantly, the mechanical stiffness of the GGMMA/CNC-SH hydrogel is mainly determined by the stoichiometric ratio between the thiol groups on CNC-SH and the methacrylate groups in GGMMA. Meanwhile, the bioactive glass nanoparticle (BaGNP)-laden hydrogels of GGMMA/CNC-SH showed a sustained release of therapeutic ions in simulated body fluid *in vitro*, which extended the bioactive function of hydrogel matrix. Furthermore, the suitability of the GGMMA/CNC-SH formulation as biomaterial resin to fabricate digitally designed hydrogel constructs *via* digital light processing (DLP) lithography printing was evaluated.

1. Introduction

Injectable and *in situ* crosslinkable hydrogels have shown immense promise to function as delivery vehicles of biotherapeutic agents for on-site therapy (Chen et al., 2019; Cheng et al., 2020; Wu et al., 2019; Wu et al., 2020). In the past decade, injectable hydrogels prepared by natural–origin polymers like gelatin, chitosan, or alginate, have attracted arising attention due to their biocompatibility and outstanding matrix properties mimicking the native extracellular matrix (Bidarra et al., 2014; Malafaya et al., 2007; Nawaz et al., 2021; Wang et al., 2021). In the family of biopolymers derived from lignocellulosic biomasses of large availability, cellulosic nanomaterials and hemicellulose biopolymers both have been widely used as building blocks in constructing hydrogels, highlighting competitive niches such as the chemical versatility with ease of modifications, high water retention properties, and non-cytotoxicity (Hynninen et al., 2018; Markstedt et al., 2017).

In the fabrication of injectable hydrogels, the crosslinking method plays a core role in resulting mechanically strong and robust hydrogels. Physical crosslinking strategies by adopting ionic-, pH- or thermal-stimulus responsive polymers, as well as chemical crosslinking strategies including Schiff's base formation, Michael addition, enzymatic crosslinking, or photo-induced polymerization, are commonly engaged depending on the actual application scenarios (Balakrishnan et al., 2014; Hou et al., 2018; Jabeen et al., 2017; Jin et al., 2010; Lin et al., 2015; Park et al., 2014; Zhang et al., 2014). As an external stimulus-responsive fabrication strategy, the photo-induced crosslinking, *via* a mechanism of either free-radical chain polymerization or orthogonal step-growth of thiol-ene 'click' addition, has been well accepted as an approach with great convenience in fabricating injectable hydrogels thanks to its rapid polymerization kinetics with minimal heat generation (Hu et al., 2012; Liu et al., 2017). In this context, natural polymers of various origins have been chemically modified with such a photo-

* Corresponding author at: Laboratory of Natural Materials Technology, Åbo Akademi University, Henrikinkatu 2, Turku FI 20500, Finland.
E-mail address: xwang@abo.fi (X. Wang).
[1] Q. Wang and W. Xu equally contributed to the present work.

https://doi.org/10.1016/j.carbpol.2021.118780
Received 1 August 2021; Received in revised form 24 September 2021; Accepted 13 October 2021
Available online 18 October 2021

reactive moiety to facilitate their derivatives as photo-crosslinkable biomaterials, *e.g.*, gelatin, hyaluronic acid, sericin, or ulvan methacryloyl (Le et al., 2018; Ning et al., 2019; Qi et al., 2018). In the category of biomass-derived hemicelluloses, we have earlier reported a facile synthesis of methacrylated galactoglucomannan (GGMMA) that showed great UV-crosslinking ability through free-radical chain polymerization, as well as the formulation of cellulose nanofiber with GGMMA as an auxiliary biopolymer for curing the hydrogels in light-assisted, hydrogel-extrusion 3D printing of the as-formulated biomaterial inks (Xu et al., 2019). Due to its reaction kinetics, free-radical chain polymerization is challenged by oxygen inhibition and in general would lead to heterogeneity of local network structures of GGMMA, resulting in a mismatch between bulk and local mechanical property of the hydrogel (Ligon et al., 2013; Lim et al., 2016, 2020; Seiffert, 2017b; Sunyer et al., 2012). In this perspective, the photo-induced thiol-ene 'click' chemistry outperforms as it provides advantages such as high conversion rate and selectivity, less oxygen inhibition, and formation of homogeneous hydrogel networks with manipulating mechanical properties (Hoyle and Bowman, 2010; Seiffert, 2017b; Yilmaz and Yagci, 2020).

Therefore, a thiolated crosslinker containing thiol moieties is needed to form a homogenous network with GGMMA through thiol-ene addition. Cellulose nanocrystals (CNC) are unique rod-like cellulosic nanomaterials that have received significant interest due to their mechanical, optical, chemical, and rheological properties (Eyley and Thielemans, 2014; Thomas et al., 2018). Previously, the synthesis of thiolated CNC (CNC-SH) was reported *via* the engraftment of L-cysteine to oxidized CNC (CNC-CHO) by reductive amination (Ruan et al., 2016). In addition, CNC has been popularly exploited as a high-performance reinforcement nanofiller for interpenetrating the polymer networks (De France et al., 2016; Domingues et al., 2014; Hynninen et al., 2018). Inspired by these peer studies, we proposed the fabrication of an injectable hydrogel with GGMMA and CNC-SH as building blocks through thiol-ene addition with the advantages of rapid photo-crosslinking kinetic and homogenous hydrogel structure. Within this initiative to develop all-polysaccharide nanocomposite hydrogels, the CNC-SH would function as both a crosslinker and a reinforcing nanofiller in the polymer network of GGMMA. By adjusting the stoichiometric ratio between thiol and ene moieties in respective CNC-SH and GGMMA, the mechanical properties of the hydrogels would be greatly adjusted. Meanwhile, the injectable GGMMA+CNC-SH hydrogel is applicable to establish the localized and sustained release of the therapeutic agents *in situ*. To extend the biofunctionality of the GGMMA+CNC-SH hydrogel, bioactive glass nanoparticles (BaGNP) were further encapsulated in the injectable hydrogel formulation to investigate the release of therapeutic ions of Si, Ca, or Cu through the hydrogel matrix. In addition, the formulated photo-crosslinkable GGMMA+CNC-SH inks could also meet the requirements for the digital light processing (DLP) 3D printing of hydrogel. The feasibility to fabricate the GGMMA+CNC-SH hydrogel *via* DLP printing offers great potential for future exploiting in various biomedical applications ranging from wound dressing to tissue engineering scaffolds.

2. Materials and method

2.1. Materials

Avicel PH-101 (microcrystalline cellulose, MCC) and tetraethyl orthosilicate (TEOS, 99%) were purchased from Fluka. Sulfuric acid (H_2SO_4, 95%) and phosphate buffered saline tablets (PBS, 100 mL) were purchased from VWR Chemicals BDH. Sodium metaperiodate ($NaIO_4$, 99%), sodium cyanoborohydride ($NaBH_3CN$, 95%), methacrylic anhydride (94%), 2-Hydroxy-4′-(2-hydroxyethoxy)-2-methylpropiophenone (Irgacure 2959, 98%), lithium phenyl-2,4,6 trimethylbenzoylphosphinate (LAP, 95%), L-cysteine (98%), hydroxylamine hydrochloride ($NH_2OH{\cdot}HCl$) and tartrazine (85%) were purchased from Sigma-Aldrich. Acetic acid glacial and sodium hydroxide were purchased from Fisher Scientific UK. GGM (Mn = 9 kDa) was obtained by hot water extraction and the chemical composition was listed in Table S3 (Xu et al., 2019). *Endo*-1,4 β-Mannanase (*Cellvibrio japonicas*, 5000 U/mL) was purchased from Megazyme Ltd. Simulated body fluid (SBF) was prepared according to the previously reported method (Kokubo and Takadama, 2006).

2.2. Synthesis of CNC-SH, GGMMA and BaGNP

CNC was prepared by H_2SO_4 (64 wt%) hydrolysis of MCC with a solid/liquid ratio of 1 g/10 mL at 45 °C for 1 h. After dialysis against deionized water (cut-off 12–14 kDa), aldehyde groups were introduced to CNC by $NaIO_4$ oxidation according to Sun's method (Sun et al., 2015). Briefly, $NaIO_4$ was added into CNC suspension (0.5 wt%) with a mass ratio of 4:1 ($NaIO_4$: CNC). The pH of the suspension was adjusted to 3.5 using acetic acid followed by reaction at 45 °C for 4 h in a dark place. The aldehyde group content of CNC-CHO was determined by titration of the HCl release during the oxime reaction with $NH_2OH{\cdot}HCl$ following the procedure reported by Alam et al. (Alam and Christopher, 2018). L-cysteine was further grafted onto the CNC-CHO through a reductive amination reaction. In short, L-cysteine and $NaBH_3CN$ were added into a CNC-CHO suspension (0.58 wt%) with a mass ratio of 8.47: 3.5: 1 (L-cysteine: $NaBH_3CN$: CNC-CHO). The pH of the suspension was adjusted to 4.5 using acetic acid followed by reaction at 45 °C for 24 h in a dark place. The resulting L-cysteine grafted CNC-SH was further dialyzed and stored under a nitrogen atmosphere. The as-synthesized CNC-SH was characterized by TEM and its degree of substitution (DS) was further quantitatively agreed with elemental analysis and liquid-state ^{13}C NMR, as detailed in Supplementary Materials. GGMMA was synthesized by reacting methacrylic anhydride with GGM according to a method reported by Xu et al. (2019). The degree of methacryloylation (DM: 0.9 mmol/g) and molecular weight (Mn = 16 kDa) of the obtained GGMMA was quantified using ^1H NMR and HPLC-SEC, respectively, as displayed in Supplementary Materials. The BaGNP samples (BaGNP with a nominal composition: 70SiO_2-30CaO-0CuO in mol% and the copper-doped Cu-BaGNP with a nominal composition of 70SiO_2-25CaO-5CuO in mol %) were synthesized according to a modified protocol reported by Zheng et al. (2017). The as-prepared BaGNP samples were characterized by TEM and SEM-EDXA (EDXA, LEO Gemini 1530 with a Thermo Scientific UltraDry Silicon Drift Detector, X-ray detector by Thermo Scientific).

2.3. Formulation of UV crosslinkable GGMMA/CNC based hydrogel precursors and hydrogel fabrication

The UV crosslinkable hydrogel precursors were prepared by dissolving GGMMA (2 wt%) and photoinitiator (0.1–0.5 wt% Irgacure 2959 or 0.25 wt% LAP) into the CNC suspensions (1 and 2 wt% CNC-CHO or 1, 2, and 3 wt% CNC-SH). The hydrogel precursors were thoroughly mixed by a vortex for 5 min. The hydrogel discs were fabricated through photopolymerization by transferring hydrogel precursors into transparent cylindrical moulds (diameter: 8 mm and height: 4.6 mm) and curing by a UV-LED (120 mW cm^{-2}, 365 nm, bluepoint LED eco, The Hönle Group) for 300 s. The fabricated GGMMA/CNC hydrogels were kept in PBS buffer prior to testing (Scheme 1).

2.4. Rheological behaviors of the formulated hydrogel precursors

The rheological profiles of hydrogel precursors of GGMMA+CNC-SH were registered by an Anton Paar Physica MCR 702 rheometer (Anton Parr GmbH) using a plate-plate geometry (25 mm diameter) with a gap distance of 0.5 mm (a coaxial double gap geometry DG26.7 was used to measure the 2% GGMMA solution) at 25 °C. The viscosity curves of the hydrogel precursors were recorded by shear flow measurement with a shear rate of 0.1 to 1000 s^{-1} with 1 s per data point. Oscillatory amplitude sweep was performed under a strain range from 0.1 to 500% with a constant frequency of 1 Hz. Photo-rheology profiles were

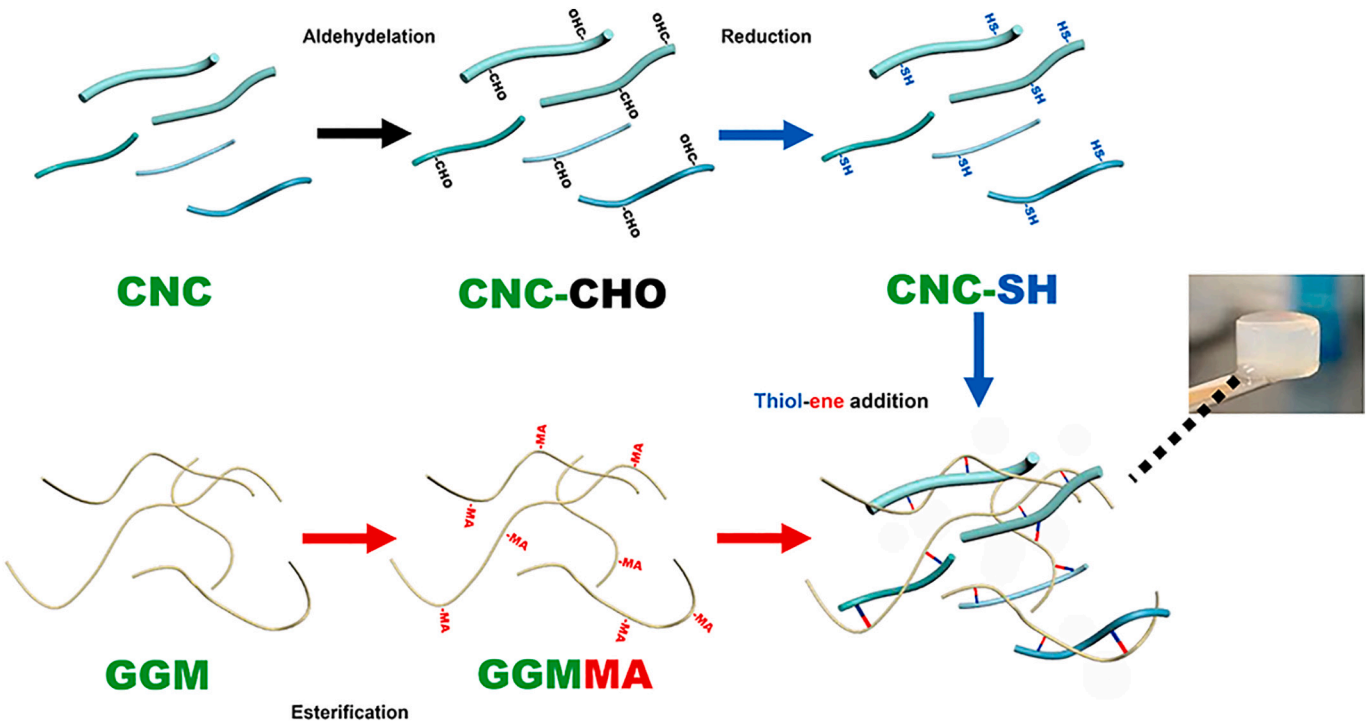

Scheme 1. Illustration of the hydrogel fabrication. CNC was isolated from the MCC and oxidized to introduce aldehyde followed by reductive amination to graft SH moiety; GGM was isolated from the tree and esterification was performed to introduce MA moiety. Hydrogel was obtained through light-induced thiol-ene addition.

measured under oscillation mode with a gap distance of 0.2 mm at a constant oscillatory strain and frequency of 0.1% and 1 Hz, respectively. The tested samples were irradiated upon a light source (365 nm or 405 nm) starting at 60 s of the measurements. The change in storage modulus was recorded. The measurements were carried out in triplicate.

2.5. Mechanical properties of the GGMMA+CNC-SH hydrogels

Compression measurements of hydrogel discs were performed by a universal tester Instron 4204 (Instron). Young's moduli of the GGMMA+CNC-SH hydrogels were calculated based on extrapolating and linear fitting of the elastic region of the stress-strain curves (Xu et al., 2019). 3 hydrogel discs of each formulation were prepared for the compression measurement. Statistical analysis was performed using the GraphPad Prism 9 software by a one-way ANOVA analysis. A Tukey test with significance level of 0.05 was apllied for the analysis.

2.6. In vitro enzymatic degradation study

In vitro enzymatic degradation of the fabricated hydrogels was performed in an air bath shaker (Boekel Scientific) at 37 °C. Briefly, hydrogels (40 mg) of different compositions (2% GGMMA, 2% GGMMA+1% CNC-CHO, and 2% GGMMA+1/2/3% CNC-SH) were immersed in a digestion liquid containing a mixture of 475 μL of PBS buffer and 25 μL of *endo*-1,4-β-Mannanase (5000 U/mL) in sealed bottles. The bottles were taken out at time points of 0.5, 1, 2, 3, 5, and 7 days and boiling for 10 min to deactivate the enzyme. The soluble carbohydrate content of the supernatant was analyzed to indicate the degradation of GGMMA (Sundberg et al., 1996). 3*6 parallel samples of each hydrogel formulation were prepared for the experiments, and 3 parallel samples were analyzed for soluble carbohydrate content at each time point.

2.7. Therapeutic ion dissolution from the BaGNP-laden GGMMA+CNC-SH hydrogel

Both BaGNP and Cu-BaGNP in weight percentages of 0.4, 1, and 2 were doped into the hydrogel precursors of 2% GGMMA+2% CNC-SH, respectively. The BaGNP-laden GGMMA+CNC-SH hydrogels were fabricated using the same protocol as described in the above section.

For the ion dissolution test, BaGNP-laden hydrogels (225 mg) were immersed in SBF (15 mL) in airtight polyethylene containers followed by placing in an incubating orbital shaker at 37 °C with agitation at 100 rpm. The samples were incubated for a total period of 7 or 14 days and 1 mL of immersion solution was sampled at 1 d (day), 3 d, 5 d, 7 d, 11 d and 14.5 d. Afterwards, 1 mL fresh SBF was replenished for consecutive immersion. The ionic concentrations of Ca and Si ions in the sampled solution were analyzed with an inductively coupled plasma optical emission spectrometer (ICP-OES) (Optima 5300 DV, Perkin Elmer, Shelton, CT). At the end of the immersion test, the hydrogels were collected from the SBF, washed extensively with deionized water, frozen in liquid nitrogen and eventually lyophilized to obtain the corresponding cryogels. The surface morphology and elemental analysis of the scaffold were characterized with SEM-EDXA. All experiments were carried out in triplicate.

2.8. DLP printing of honeycomb structure hydrogels with the BaGNP-laden hydrogel precursor of 2% GGMMA+1% CNC-SH

The honeycomb structure of hydrogels was demonstrated by a DLP 3D printer (M-One Pro 30, wavelength of 405 nm) equipped with a digital micromirror device (resolution: 1920 × 1080). The CAD model of the honeycomb construct was designed by Fusion 360 software and transfer into the digital pattern by the XMaker V2.7.1 software. Hydrogel precursors of 1 wt% CNC-SH, 2 wt% of GGMMA and 0.25 wt% LAP with or without 0.4 wt% 5Cu-BaGNP and 0.4 mM tartrazine were loaded onto the printing bed and fabricated into a hexagonal structure under light exposure. The layer height of the printer construct was set at 35 μm.

3. Results and discussion

3.1. Synthesis and characterizations on CNC-SH and GGMMA

The CNC-SH was synthesized *via* the route illustrated in Fig. 1a. After being surface modified with pendant cysteine groups, CNC-SH maintained the rod-like nanomorphology with an average length of 145 nm and diameter of 5 nm, as observed in the TEM image. The chemical modification in the molecular structure of the CNC was quantitatively determined by the liquid-state quantitative ^{13}C NMR (King et al., 2018). As shown in Fig. 1b, signals of anomeric carbon (C1, 101 to 105 ppm) and C2 to C6 (60 to 82 ppm) of CNC samples can be attributed to the featured signals of cellulose. After the $NaIO_4$ oxidation, the bond between C2 and C3 was selectively cleaved in formation of dialdehyde (C2′ and C3′ at 165 to 167 ppm) in sites. Meanwhile, the signals of C2″ and C3″ were detected at 93 and 98 ppm, respectively, attributed to the hemiacetal formation of the aldehyde group (Amer et al., 2016; Münster et al., 2017; Nypelö et al., 2021). The DS of the aldehyde group (DS = 0.26) in CNC-CHO was computed by the comparison of sum signal integration of C2′, C3′, C2″, and C3″ to C1 as displayed in Fig. 1b, which is in line with the DS of 1.45 mmol/g calculated by titration. As shown in Fig. 1b, the grafting of L-cysteine to CNC-CHO was confirmed by the appearance of a new signal at 172 to 173 ppm, which is attributed to the carboxyl carbon (C9) of L-cysteine. The DS of L-cysteine (DS = 0.20) in CNC-SH was determined by the integral comparison of signal of the C9 to that of C1 and C9 as displayed in Fig. 1b, which is in line with the DS value (DS = 1.04 mmol/g) that is calculated from the nitrogen content in CNC-SH by elemental analysis as shown in Table S1 and S2. It is noted that the DS of L-cysteine appears smaller than the DS of aldehyde in CNC-CHO. The signals attributed to the dialdehyde completely disappeared in the ^{13}C NMR spectra of CNC-SH, as the remaining aldehydes were further reduced into the hydroxyls by $NaBH_3CN$ in the reductive amination. Compared with the solid-state ^{13}C NMR analysis on the L-cysteine grafted CNC carried by Li et al., the employment of a mixture of ionic liquid tetrabutylphosphonium acetate ([P4444][OAc]) and DMSO-d_6 (1:4 w/w) as in liquid-status ^{13}C NMR facilitates the quantitative analysis to the chemical modifications that are induced in the CNC samples (Li et al., 2019). This is critical information to register for precise formulation control in realizing on/off stoichiometric thiol-ene chemistry between CNC-SH and GGMMA. The chemical structure and ^{1}H and ^{13}C NMR spectra of GGMMA are presented in Fig. 1c. The GGMMA with such a DM (0.9 mmol/g) was chosen to fabricate hydrogels with CNC-SH through thiol-ene chemistry, taking into balance between the decent DM and good solubility of the biopolymer under consideration.

3.2. Rheological properties and photo-crosslinking kinetics of hydrogel precursors of GGMMA+CNC-SH and mechanical property of photocured hydrogels

In making high-performance injectable hydrogels, the hydrogel precursors of GGMMA+CNC-SH are critically expected to show outstanding injectability (shear-thinning behavior) and rapid crosslinking kinetics. The rheological properties and photo-crosslinking kinetics of the hydrogel precursors of GGMMA+CNC-SH were promptly assessed. As a soluble polysaccharide, 2% GGMMA solution showed a low viscosity and behaved like a Newtonian liquid at high shear rates, as shown in Fig. 2a. The addition of CNC-SH into 2% GGMMA solution drastically increased the viscosity of the resulted hydrogel precursors. The viscosity also increased with the increase of the CNC-SH concentration. Meanwhile, in comparison to the pristine CNC-SH solution, the incorporation of GGMMA increased the zero-shear viscosity of the hydrogel precursors of GGMMA+CNC-SH. All the hydrogel precursors presented a characteristic shear-thinning behavior exhibiting a viscosity reduction as they flow upon shear. Viscoelastic properties of the GGMMA+CNC-SH hydrogel precursors were analyzed through amplitude sweep, the storage and loss modulus (G′ and G″) verse shear stress were piloted as displayed in Fig. 2b. The hydrogel precursors showed rather weak viscoelasity with the low G′ and the flow stress (shear stress at the crossover point of G′ and G″) were lower than 10 Pa. The G′ and flow stress of the hydrogel precursors increased with the increase of CNC-SH concentration. The low viscosity and viscoelasticity indicated a good flowability of the hydrogel precursors, facilitating their extrusion process for injectable hydrogel or recoating process in DLP printing (Bertsch et al., 2019; Lim et al., 2020).

Nevertheless, the injectable hydrogel is required to instantly form gel conforming to the desired geometry at the application site and to supply mechanical support after injection (Bertsch et al., 2019). Sufficiently rapid gelation kinetics are imperative for gelation of the hydrogel precursors. Here, the GGMMA+CNC-SH based hydrogel precursors were subjected to photo-initiated crosslinking *via* the high-efficacy thiol–ene chemistry, which is expected to present a faster crosslinking speed and to result in a more homogenous microscopic structure within the gel, in comparison to the free-radical chain polymerization that is the case for the photo-initiated crosslinking of GGMMA (Yu et al., 2020). The crosslinking kinetics of the formulations was assessed using photo-rheology. As shown in Fig. 2c, the crosslinking of all the hydrogel precursors of GGMMA+CNC-SH was initiated immediately upon UV irradiation as indicated by the dramatic increase in G′. Meanwhile, the hydrogel precursors of GGMMA+CNC-SH showed a rapid crosslinking kinetics with the G′ value levelling off within 30 s to reach the maximum value of G'_{max}. In contrast to the G'_{max} of GGMMA after crosslinking, the G'_{max} of the hydrogel precursors of GGMMA+CHC-CHO with different CNC-CHO content further increased. It is noteworthy that the G′ tends to be even higher when the same content of CNC-CHO was systemically replaced by CNC-SH. It is indicative that CNC-CHO only acts as a reinforcing component instead of contributing crosslinking efforts (Sampath et al., 2017). The result is consistent with the previous observation that G′ of hydrogels reinforced with chemically bound CNC was higher than neat CNC reinforced hydrogels at the same loading (Yang et al., 2013). This result is likely attributed to CNC-SH being both physically entrapped within and chemically bound to the hydrogel network, thus serving as a reinforcing agent and a crosslinker. The dosage of photoinitiator plays a vital role in crosslinking kinetics, where the G′ of 2% GGMMA+2% CNC-SH hydrogel increased more rapidly with the increase of the Irgacure 2959 concentration, as shown in Fig. S1.

After gelation, the hydrogel is expected to provide adequate mechanical support and robustness as demanded at the specific application site. The compressive Young's moduli of the hydrogel discs are displayed in Fig. 2d. The rod-like CNC-CHO as an effective nanofiller significantly enhanced the mechanical property of the GGMMA hydrogel, where the compressive strength increased drastically after adding 1% of CNC-CHO. In addition, the physically entrapped and chemically bound CNC-SH exhibited even better mechanical reinforcement performance than CNC-CHO. Compared with the GGMMA+CNC-CHO hydrogels that were photo-polymerized through the free-radical chain polymerization to crosslink the GGMMA, the GGMMA+CNC-SH hydrogels would provide a better spatial network homogeneity within the gel through the orthogonal step-growth mechanism of thiol-ene addition (Grigoryan et al., 2019). The relatively homogeneous network structure shall consequently result in a better match between bulk and local property, and thus influence the mechanical properties (Sunyer et al., 2012). By varying the compositional ratio between GGMMA and CNC-SH, Young's moduli of hydrogels could be tailored in the spectrum of 1.43 to 12.35 kPa. These as-measured stiffness values fall into the range (5–40 kPa) of the mechanical stiffness of hydrogel matrix suitable for cell culture study of different types, including pre-osteoblast, fibroblast, and cardiovascular cells (Nemir and West, 2010). Potentially, the GGMMA+CNC-SH hydrogels could function as a candidate biomaterial system for *in vitro* cell culture studies. Not surprisingly, the 2% GGMMA+2% CNC-SH hydrogel with an on-stoichiometry molar ratio of MA: SH close to 1:1, showed the highest Young's modulus among all the hydrogels. As a

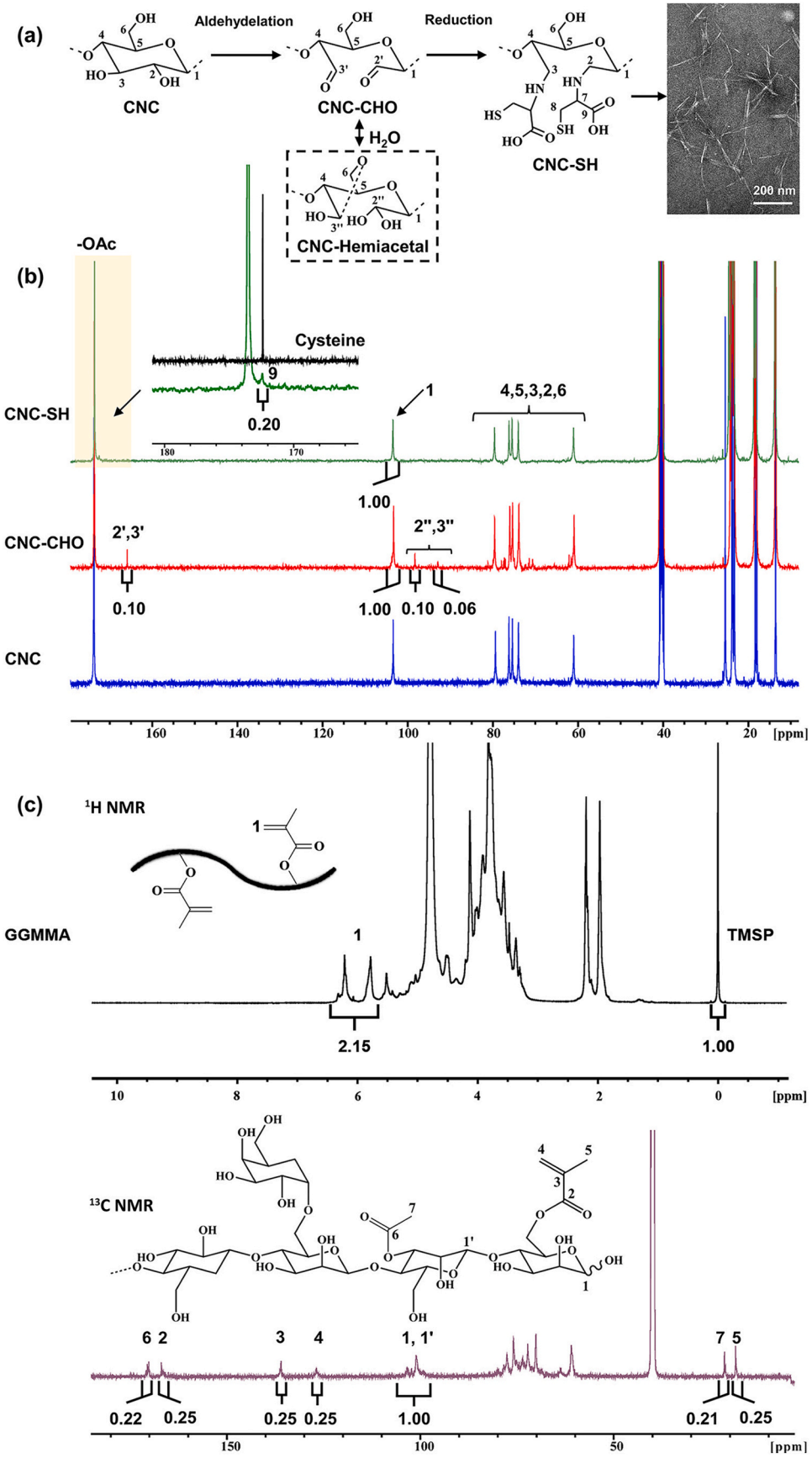

Fig. 1. (a) Synthetic route and TEM image of CNC-SH, (b) quantitative ^{13}C NMR spectra of CNC, CNC-CHO, CNC-SH samples and L-cysteine, and (c) quantitative ^{1}H and ^{13}C NMR spectra of GGMMA.

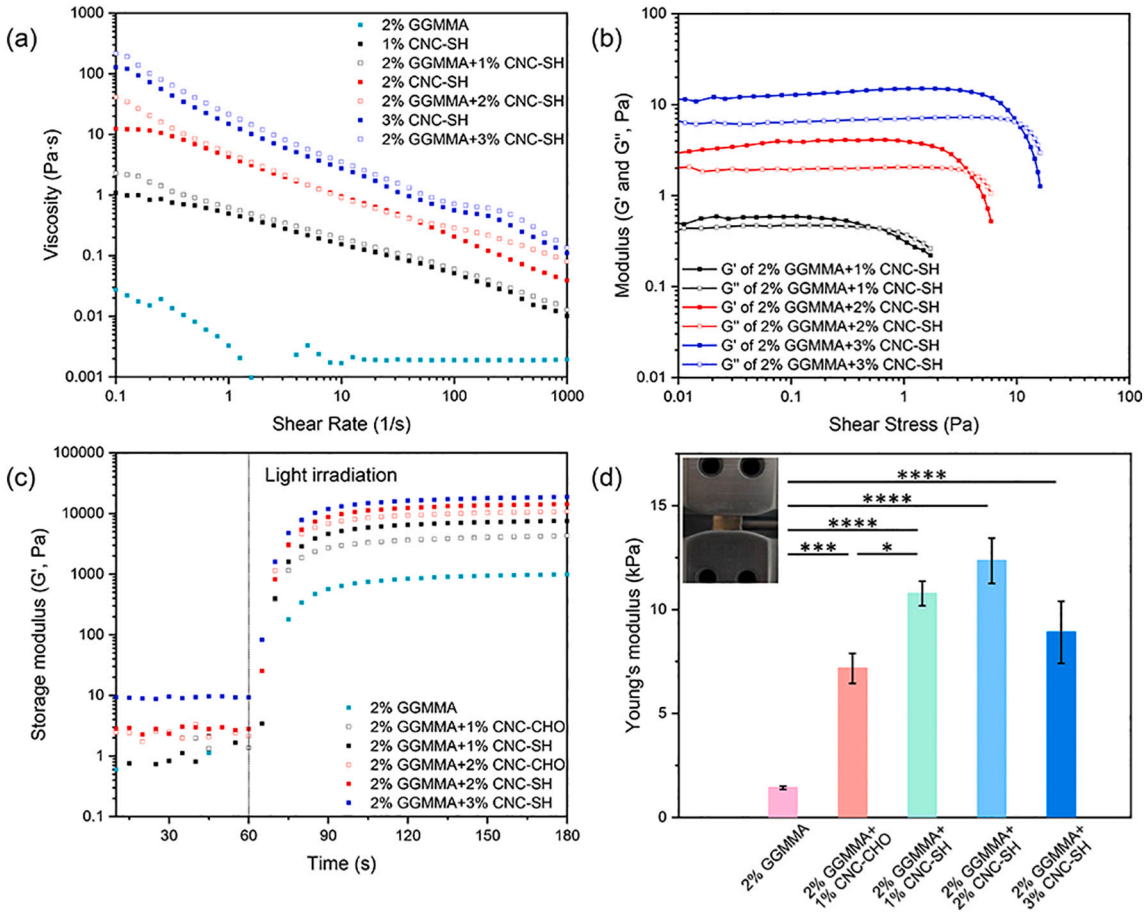

Fig. 2. (a) Flow curves, (b) viscoelastic behavior, and (c) photo-rheology profiles of the hydrogel precursors (0.5 wt% Irgacure 2959 as photoinitiator), and (d) Young's modulus of GGMMA/CNC hydrogels. **** indicates $p < 0.0001$, *** indicates $p = 0.0008$, * indicates $p = 0.02$. Error bars are standard error of the mean.

comparison, the 2% GGMMA+3% CNC-SH with a higher MA: SH ratio of 1:1.7 showed higher viscoelasticity (Fig. 2c) with higher CNC-SH loading, but showed a decreased mechanical property no matter of the excess amount of CNC-SH as reinforcement. This could be attributed to an almost equal amount of thiol and methacrylate groups resulting in no excess off-stoichiometry and maximizing polymer mechanical properties (Carlborg et al., 2011).

3.3. *Mannanase mediated degradation of the GGMMA/CNC hydrogel in PBS buffer*

Considering the in stimuli-responsive or controlled therapeutic delivery, it is imperative to regulate the degradation of the construct hydrogel systems. However, human body lacks the enzymes that can degrade lignocellulosic biopolymers. Thus, enzyme immobilization in or secretion to the matrix is typically required. To address this perspective, the enzymatic degradation of GGMMA+CNC-SH hydrogels was evaluated *in vitro* with the *endo*-1,4-β-mannanase from *Cellvibrio japonicas* in PBS buffer. The applied mannanase could actively and randomly hydrolyze (1, 4)-β-D-mannosidic linkages at pH 7.0. Owing to the hygroscopic property and porosity structure of the hydrogels, mass transfer of enzyme is easily undergoing between the hydrogel and the surrounding aqueous media facilitating the degradation process (Gorgieva and Kokol, 2012). The degradation kinetics of GGMMA was revealed by quantifying the soluble carbohydrate contents by gas chromatography, as shown in Fig. 3. Overall, GGMMA/CNC hydrogels presented faster degradation kinetics than the pristine GGMMA hydrogels. The physically entrapped CNC-CHO in 2% GGMMA+1% CNC-CHO hydrogel might sterically block the crosslinking of GGMMA to a certain extent

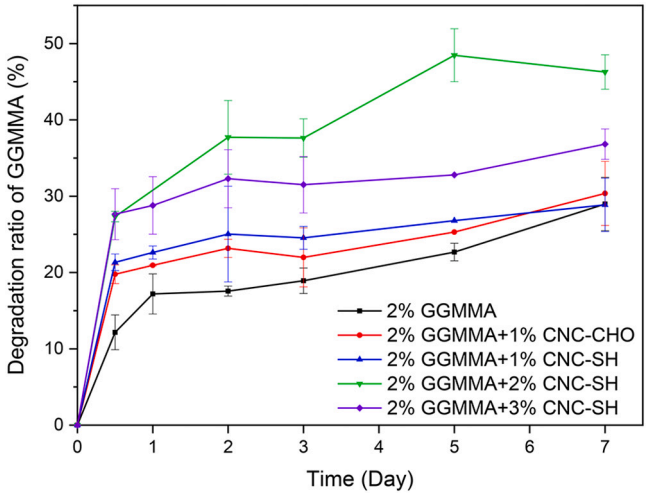

Fig. 3. Mannanase-mediated degradation of GGMMA in GGMMA/CNC based hydrogels.

(Yang et al., 2013). It is speculated that the steric spacing of CNC in the matrix would result in a relatively loose structure of GGMMA, which presumably facilitated faster mannanase diffusion in/out the hydrogel system. The hydrolysis kinetics of GGMMA was further enhanced in GGMMA+CNC-SH hydrogel, which might be attributed to the improved local homogeneity resulting from orthogonal step-growth polymerization of thiol-ene addition (Seiffert, 2017a). The on-stoichiometry thiol-

ene hydrogel of 2% GGMMA+2% CNC-SH presented the fastest hydrolysis kinetic, reaching around 29% GGMMA degradation in half-a-day and around 50% of GGMMA after 7 days. Meanwhile, the degradation kinetics of GGMMA in 2% GGMMA+3% CNC-SH hydrogel fell off the track of 2% GGMMA+2% CNC-SH after half-a-day hydrolysis. It is suspected that excess CNC-SH covering the GGMMA surface and blocking the enzyme binding site due to the intrinsic interaction between cellulose and hemicellulose (Lucenius et al., 2019). Nevertheless, the addition of CNC-CHO or covalent-bound CNC-SH could tailor the hydrogel degradation for potentially achieving a controlled therapeutic delivery manipulation.

3.4. BaGNP laden GGMMA+CNC-SH hydrogels and in vitro sustained release of therapeutics ions in SBF

Supported by the sustained ion release profiles and the confirmed none cytotoxicity in the culture of various cell lines, BaGNP has been suggested as promising nano-sized fillers to develop nanocomposites both for bone regeneration and wound healing, especially Cu-BaGNP (Wang et al., 2016; Weng et al., 2017). The two sol-gel-derived BaGNP samples, BaGNP and Cu-BaGNP, are highly dispersive in water and display as mono-dispersed solid spheres with a diameter around 400 nm as determined from TEM and SEM imaging in Fig. 4a. The addition of Cu precursor resulted in no distinct variations in surface morphology between the BaGNP and Cu-BaGNP, as the comparatively low doping content of Cu in Cu-BaGNP. Semi-quantitative surface element analysis was carried out using the EDXA in conjugation with SEM imaging to determine the composition of the BaGNP samples, as presented in Fig. 4a. Both BaGNP and Cu-BaGNP showed a significant deviation from their respective nominal composition, and the actual contents of CaO and CuO were significantly lower than the nominal values: 4.53 mol% CaO was confirmed in the final composition of BaGNP, and 0.41 mol% CuO was further introduced as a competing dopant with 4.17 mol% CaO for Cu-BaGNP. The result is in line with the previous study, owing to the limited active sites in the silicate particles, only a certain amount of Ca or/and Cu ions are adsorbed in the Stöber process and eventually integrated into the network structure as dopants in the calcinated BaGNPs (Zheng et al., 2017). In line with the strategy mentioned above, the hydrogel precursors of GGMMA+CNC-SH were then proposed to construct a UV-curable nanocomposite hydrogel of polysaccharides and BaGNP as a delivery system aiming to provide a sustained release of therapeutic ions including Si, Ca, or/and Cu ions.

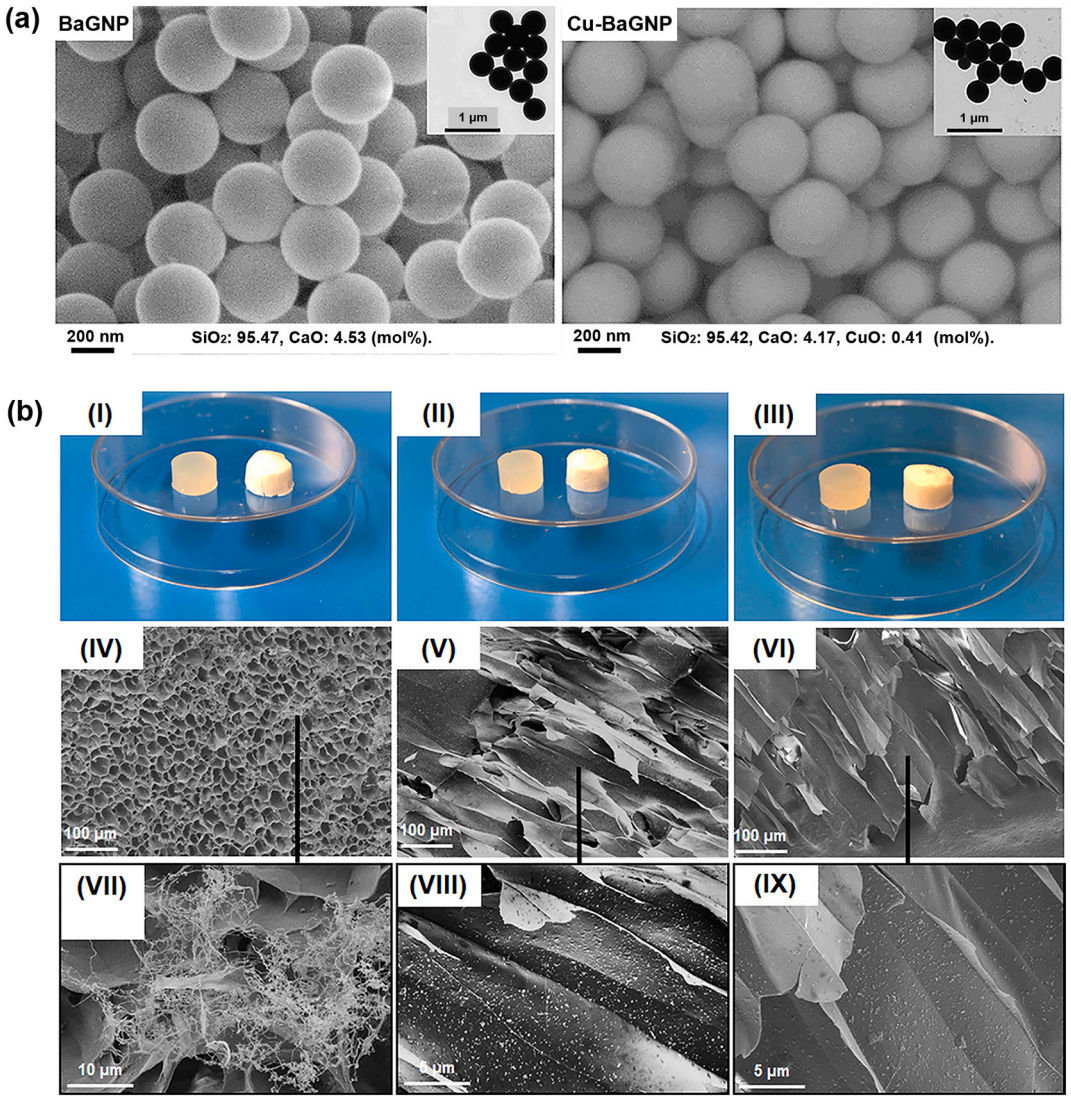

Fig. 4. (a) SEM and TEM images of BaGNP and Cu-BaGNP samples. (b) Hydrogel and cryogel fabricated by 2% GGMMA+2% CNC-SH, 2% GGMMA+2% CNC-SH+2% BaGNP, and 2% GGMMA+2% CNC-SH+2% Cu-BaGNP (I to III); SEM cross-sections of 2% GGMMA+2% CNC-SH (IV and VII), 2% GGMMA+2% CNC-SH+2% BaGNP (V and VIII), and 2% GGMMA+2% CNC-SH+2% Cu-BaGNP (VI and IX) cryogels.

The hydrogel of 2% GGMMA+2% CNC-SH was selected as the carrier system matrix due to its outstanding mechanical strength and relatively homogenous structure. BaGNP or Cu-BaGNP was introduced at a dosage of 0.4%, 1%, or 2% to prepare the nanocomposite hydrogels of GGMMA+CNC-SH+BaGNP. The release profiles of Si, Ca, and Cu ions/species from these nanocomposite hydrogels were registered in SBF for up to 7 or 14 days, as shown in Fig. 5. BaGNP and Cu-BaGNP laden hydrogels showed a similar Si release profile, and the released Si concentration is mainly related to the BaGNP loading in the hydrogel. A sustained release of Si ions/species was observed during the evaluation, in which an almost linear increase within 7 days, as shown in Fig. 5a and c. To be noticed, BaGNP and Cu-BaGNP alone showed rapid Si release profiles in the first 3 days, then a slow release in the next 11 days (Zheng et al., 2017). This indicates that the GGMMA+CNC-SH hydrogel, as a delivery matrix, could impact the release of Si and enable a sustainable release profile. For both BaGNP laden hydrogels, a depletion of Ca ions was initially observed within the time point of 2 days and continued to increase in the late dissolution stage. This might be owing to the released Ca and P formed CaP-rich species. However, no obvious apatite-formation (typically as needle-like crystals) was observed under SEM investigation to the cross-sectioned lyophilized cryogels after immersion of dissolution test. The GGMMA+CNC-SH cryogel showed a highly porous network, as displayed in Fig. 4b (IV and VII). Still, a relatively homogeneous and spatial embedding of BaGNP in the matrix of GGMMA+CNC-SH was suggested in Fig. 4b (V and VIII for 2% BaGNP-laden cryogel; and VI and IX for 2% Cu-BaGNP-laden cyrogel). Besides, no detectable concentration of Cu ion was found in SBF by the ICP-OES analysis (or the concentration of Cu ion is lower than the detection limit). However, this did not imply that no Cu ions were dissolved from the embedded Cu-BaGNP in the hydrogel matrix. It is speculated that the dissolved Cu ions were adsorbed onto the GGMMA and CNC-SH matrix through the ionic complexation with the presence of sulfate half ester groups on the surface of CNC and carbonyl groups in grafted L-cysteine.

3.5. Fabrication of GGMMA+CNC-SH hydrogels with DLP lithography printing

DLP additive manufacturing (AM) creates models in a layer-by-layer manner through photo-polymerization *via* UV or visible light. The technological dimensions of DLP 3D printing are highlighted with excellent spatial resolution in pattern fidelity and rapid fabrication speed, which has made it popular in fabricating custom-designed hydrogel constructs with biomaterial resins of different kinds (Hong et al., 2020; Shen et al., 2020; Ye et al., 2020). Preliminary, we further investigated the applicability of the hydrogel precursors of GGMMA+CNC-SH as the biomaterial resin in DLP printing. Considering the requirement on resins suitable for DLP in terms of flowability (ideally low-viscosity Newtonian fluids in recoating process), the less viscous hydrogel precursor of 2% GGMMA+1% CNC-SH was chosen as the resin to print a honeycomb structure in 1 mm height, as digitally designed in a model depicted in Fig. 6a.

In this AM technique, apart from the pixel size as defined by the photonics in the DLP printer, the printing resolution is majorly determined by the kinetics of photo-polymerization. When printing the resin of 2% GGMMA+1% CNC-SH, blurred projected pattern (over-curing layers beyond the focus plane, indicated by arrows) and excess crosslinking were observed in the honeycomb. This was caused by the 'light trespassing' associated with the weak light absorption of optically clear GGMMA+CNC-SH. Here, tunable crosslinking kinetics is necessary to improve the shape fidelity of the printed hydrogel. Commonly, a photoabsorber that functions as a light-attenuating additive is added in resin formulation to absorb excess light, *e.g.* water-soluble dyes such as

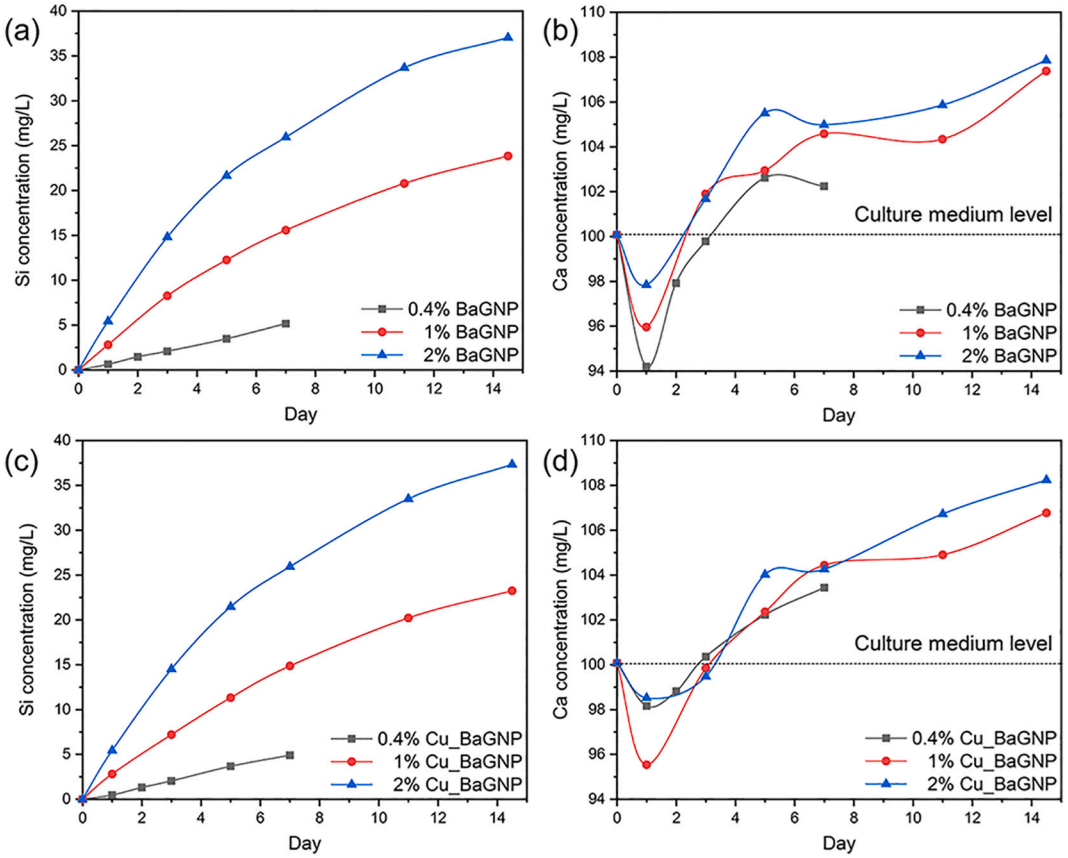

Fig. 5. Ion release profiles of BaGNP and Cu-BaGNP laden GGMMA+CNC-SH hydrogels in SBF show sustained release of (a and c) Si and (b and d) Ca ions for up to 7 or 14 days.

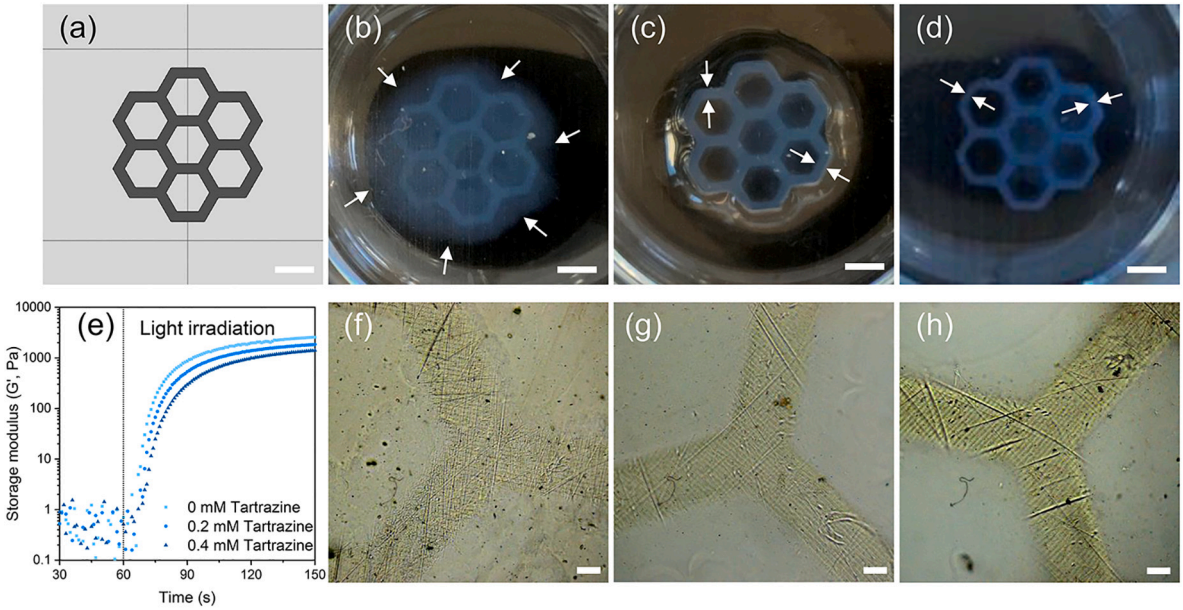

Fig. 6. (a) CAD design of a honeycomb structure, (b–d) DLP printed honeycomb construct of 2% GGMMA+1% CNC-SH, 2% GGMMA+1% CNC-SH+0.4 mM tartrazine, and 2% GGMMA+1% CNC-SH+0.4% Cu-BaGNP+0.4 mM tartrazine, (e) influence of the tartrazine concentration on the crosslinking kinetics of 2% GGMMA+1% CNC-SH, and (f–h) optical microscopy of 2% GGMMA+1% CNC-SH, 2% GGMMA+1% CNC-SH+0.4 mM tartrazine, and 2% GGMMA+1% CNC-SH+0.4% Cu-BaGNP+0.4 mM tartrazine. Scale bar: 2 mm (a–d) and 200 μm (f–h).

tartrazine, curcumin, or anthocyanin that has strong absorbance in the near-UV to visible blue light (Grigoryan et al., 2019; Yu et al., 2020). Herein, tartrazine was incorporated as a photoabsorber in 2% GGMMA+1% CNC-SH. As shown in Fig. 6e, the crosslinking kinetics of the resin was gradually inhibited with increasing the tartrazine concentration. With optimizing this parameter in the printing of the honeycomb hydrogel, 0.4 mM tartrazine was found to significantly preventing the over-curing of resins and improved the shape fidelity of the hydrogel, as shown in Fig. 6(b, c, f and g). When 0.4% Cu-BaGNP was further encapsulated in the formulation, the printed honeycomb hydrogel with sharp edges also shows good shape fidelity and a clear X-Y resolution could be observed from the microscopy images from Fig. 6h.

4. Conclusion

Through photo-clickable thiol-ene crosslinking, the methacrylated derivative of woody polysaccharide (GGMMA) together with the thiol-grafted CNC (CNC-SH) are high-performance building blocks to form an injectable and rapidly photocurable nanocomposite hydrogel. Based on on/off-stoichiometry content control of thiol:ene, the mechanical stiffness of these all wood-derived polysaccharide hydrogels was tunable within the range of 1.43 to 12.35 kPa. The on-stoichiometry thiol-ene addition guaranteed a homogenous network within the gel, which supports strong mechanical properties and a fast enzymatic degradation kinetics when incubated with mannanase. As an extended therapeutic delivery function, a sustained release of Si and Ca ions/species was achieved by embedding the BaGNP in the hydrogel of GGMMA+CNC-SH. Moreover, the GGMMA+CNC-SH formulation is suitable as biomaterial resin in DLP lithography printing to fabricate digitally designed hydrogel constructs.

CRediT authorship contribution statement

Qingbo Wang: Methodology, Investigation, Validation, Writing – original draft, Visualization, Writing – review & editing. **Wenyang Xu:** Conceptualization, Methodology, Writing – original draft, Writing – review & editing. **Rajesh Koppolu:** Investigation, Writing – review & editing. **Bas van Bochove:** Investigation, Writing – review & editing. **Jukka Seppälä:** Resources, Writing – review & editing. **Leena Hupa:** Resources, Writing – review & editing. **Stefan Willför:** Resources, Writing – review & editing. **Chunlin Xu:** Resources, Writing – review & editing. **Xiaoju Wang:** Conceptualization, Methodology, Investigation, Resources, Writing – original draft, Supervision, Project administration, Funding acquisition, Writing – review & editing.

Declaration of competing interest

The authors declare no conflicts of interest.

Acknowledgement

Qingbo Wang would like to acknowledge the financial support from the China Scholarship Council (Student ID 201907960002) and KAUTE Foundation (Project number 20190031) to his doctoral study at Åbo Akademi University (ÅAU), Finland. Xiaoju Wang would like to thank Academy of Finland (333158) as well as Jane and Aatos Erkko Foundation for their funds to her research at ÅAU. This work is also part of activities within the Johan Gadolin Process Chemistry Centre (PCC) and has used the Aalto University Bioeconomy Facilities. Luyao Wang, Yury Brusentsev, and Sara Lund are respectively acknowledged for their technical assistance on TEM, NMR, and elemental analysis. Adrian Stiller and Jaana Paananen are acknowledged for their assistance on BaGNP dissolution experiments.

Appendix A. Supplementary data

Supplementary data to this article can be found online at https://doi.org/10.1016/j.carbpol.2021.118780.

References

Alam, M. N., & Christopher, L. P. (2018). Natural cellulose-chitosan cross-linked superabsorbent hydrogels with superior swelling properties. *ACS Sustainable Chemistry & Engineering, 6*(7), 8736–8742. https://doi.org/10.1021/ACSSUSCHEMENG.8B01062

Amer, H., Nypelö, T., Sulaeva, I., Bacher, M., Henniges, U., Potthast, A., & Rosenau, T. (2016). Synthesis and characterization of periodate-oxidized polysaccharides:

Dialdehyde xylan (DAX). *Biomacromolecules, 17*(9), 2972–2980. https://doi.org/10.1021/acs.biomac.6b00777
Balakrishnan, B., Joshi, N., Jayakrishnan, A., & Banerjee, R. (2014). Self-crosslinked oxidized alginate/gelatin hydrogel as injectable, adhesive biomimetic scaffolds for cartilage regeneration. *Acta Biomaterialia, 10*(8), 3650–3663. https://doi.org/10.1016/j.actbio.2014.04.031
Bertsch, P., Schneider, L., Bovone, G., Tibbitt, M. W., Fischer, P., & Gstöhl, S. (2019). Injectable biocompatible hydrogels from cellulose nanocrystals for locally targeted sustained drug release. *ACS Applied Materials and Interfaces, 11*(42), 38578–38585. https://doi.org/10.1021/acsami.9b15896
Bidarra, S. J., Barrias, C. C., & Granja, P. L. (2014). Injectable alginate hydrogels for cell delivery in tissue engineering. *Acta Biomaterialia, 10*(4), 1646–1662. https://doi.org/10.1016/J.ACTBIO.2013.12.006
Carlborg, C. F., Haraldsson, T., Öberg, K., Malkoch, M., & van der Wijngaart, W. (2011). Beyond PDMS: Off-stoichiometry thiol–ene (OSTE) based soft lithography for rapid prototyping of microfluidic devices. *Lab on a Chip, 11*(18), 3136–3147. https://doi.org/10.1039/C1LC20388F
Chen, N., Wang, H., Ling, C., Vermerris, W., Wang, B., & Tong, Z. (2019). Cellulose-based injectable hydrogel composite for pH-responsive and controllable drug delivery. *Carbohydrate Polymers, 225*, Article 115207. https://doi.org/10.1016/j.carbpol.2019.115207
Cheng, L., Cai, Z., Ye, T., Yu, X., Chen, Z., Yan, Y., Qi, J., Wang, L., Liu, Z., Cui, W., & Deng, L. (2020). Injectable polypeptide-protein hydrogels for promoting infected wound healing. *Advanced Functional Materials, 30*(25), 2001196. https://doi.org/10.1002/adfm.202001196
De France, K. J., Chan, K. J. W., Cranston, E. D., & Hoare, T. (2016). Enhanced mechanical properties in cellulose nanocrystal-poly(oligoethylene glycol methacrylate) injectable nanocomposite hydrogels through control of physical and chemical cross-linking. *Biomacromolecules, 17*(2), 649–660. https://doi.org/10.1021/acs.biomac.5b01598
Domingues, R. M. A., Gomes, M. E., & Reis, R. L. (2014). The potential of cellulose nanocrystals in tissue engineering strategies. *Biomacromolecules, 15*(7), 2327–2346. https://doi.org/10.1021/BM500524S
Eyley, S., & Thielemans, W. (2014). Surface modification of cellulose nanocrystals. *Nanoscale, 6*(14), 7764–7779. https://doi.org/10.1039/c4nr01756k
Gorgieva, S., & Kokol, V. (2012). Preparation, characterization, and in vitro enzymatic degradation of chitosan-gelatine hydrogel scaffolds as potential biomaterials. *Journal of Biomedical Materials Research Part A, 100A*(7), 1655–1667. https://doi.org/10.1002/jbm.a.34106
Grigoryan, B., Paulsen, S. J., Corbett, D. C., Sazer, D. W., Fortin, C. L., Zaita, A. J., Greenfield, P. T., Calafat, N. J., Gounley, J. P., Ta, A. H., Johansson, F., Randles, A., Rosenkrantz, J. E., Louis-Rosenberg, J. D., Galie, P. A., Stevens, K. R., & Miller, J. S. (2019). Multivascular networks and functional intravascular topologies within biocompatible hydrogels. *Science, 364*(6439), 458–464. https://doi.org/10.1126/SCIENCE.AAV9750
Hong, H., Seo, Y. B., Kim, D. Y., Lee, J. S., Lee, Y. J., Lee, H., Ajiteru, O., Sultan, M. T., Lee, O. J., Kim, S. H., & Park, C. H. (2020). Digital light processing 3D printed silk fibroin hydrogel for cartilage tissue engineering. *Biomaterials, 232*, Article 119679. https://doi.org/10.1016/j.biomaterials.2019.119679
Hou, S., Lake, R., Park, S., Edwards, S., Jones, C., & Jeong, K. J. (2018). Injectable macroporous hydrogel formed by enzymatic cross-linking of gelatin microgels. *ACS Applied Bio Materials, 1*(5), 1430–1439. https://doi.org/10.1021/acsabm.8b00380
Hoyle, C. E., & Bowman, C. N. (2010). Thiol-ene click chemistry. *Angewandte Chemie International Edition, 49*(9), 1540–1573. https://doi.org/10.1002/anie.200903924
Hu, J., Hou, Y., Park, H., Choi, B., Hou, S., Chung, A., & Lee, M. (2012). Visible light crosslinkable chitosan hydrogels for tissue engineering. *Acta Biomaterialia, 8*(5), 1730–1738. https://doi.org/10.1016/j.actbio.2012.01.029
Hynninen, V., Hietala, S., McKee, J. R., et al.Murtomäki, L., Rojas, O. J., Ikkala, O., & Nonappa. (2018). Inverse thermoreversible mechanical stiffening and birefringence in a methylcellulose/cellulose nanocrystal hydrogel. *Biomacromolecules, 19*(7), 2795–2804. https://doi.org/10.1021/acs.biomac.8b00392
Jabeen, S., Islam, A., Ghaffar, A., Gull, N., Hameed, A., Bashir, A., Jamil, T., & Hussain, T. (2017). Development of a novel pH sensitive silane crosslinked injectable hydrogel for controlled release of neomycin sulfate. *International Journal of Biological Macromolecules, 97*, 218–227. https://doi.org/10.1016/j.ijbiomac.2017.01.014
Jin, R., Teixeira, L. S. M., Krouwels, A., Dijkstra, P. J., Van Blitterswijk, C. A., Karperien, M., & Feijen, J. (2010). Synthesis and characterization of hyaluronic acid-poly(ethylene glycol) hydrogels via Michael addition: An injectable biomaterial for cartilage repair. *Acta Biomaterialia, 6*(6), 1968–1977. https://doi.org/10.1016/j.actbio.2009.12.024
King, A. W. T., Mäkelä, V., Kedzior, S. A., Laaksonen, T., Partl, G. J., Heikkinen, S., Koskela, H., Heikkinen, H. A., Holding, A. J., Cranston, E. D., & Kilpeläinen, I. (2018). Liquid-state NMR analysis of nanocelluloses. *Biomacromolecules, 19*(7), 2708–2720. https://doi.org/10.1021/acs.biomac.8b00295
Kokubo, T., & Takadama, H. (2006). How useful is SBF in predicting in vivo bone bioactivity? *Biomaterials, 27*(15), 2907–2915. https://doi.org/10.1016/j.biomaterials.2006.01.017
Le, L. V., Mohindra, P., Fang, Q., Sievers, R. E., Mkrtschjan, M. A., Solis, C., Safranek, C. W., Russell, B., Lee, R. J., & Desai, T. A. (2018). Injectable hyaluronic acid based microrods provide local micromechanical and biochemical cues to attenuate cardiac fibrosis after myocardial infarction. *Biomaterials, 169*, 11–21. https://doi.org/10.1016/j.biomaterials.2018.03.042
Li, W., Ju, B., & Zhang, S. (2019). A green l-cysteine modified cellulose nanocrystals biosorbent for adsorption of mercury ions from aqueous solutions. *RSC Advances, 9*(12), 6986–6994. https://doi.org/10.1039/c9ra00048h
Ligon, S. C., Husár, B., Wutzel, H., Holman, R., & Liska, R. (2013). Strategies to reduce oxygen inhibition in photoinduced polymerization. *Chemical Reviews, 114*(1), 577–589. https://doi.org/10.1021/CR3005197
Lim, K. S., Galarraga, J. H., Cui, X., Lindberg, G. C. J., Burdick, J. A., & Woodfield, T. B. F. (2020). Fundamentals and applications of photo-cross-linking in bioprinting. *Chemical Reviews, 120*(19), 10662–10694. https://doi.org/10.1021/ACS.CHEMREV.9B00812
Lim, K. S., Schon, B. S., Mekhileri, N. V., Brown, G. C. J., Chia, C. M., Prabakar, S., Hooper, G. J., & Woodfield, T. B. F. (2016). New visible-light photoinitiating system for improved print Fidelity in gelatin-based bioinks. *ACS Biomaterials Science and Engineering, 2*(10), 1752–1762. https://doi.org/10.1021/ACSBIOMATERIALS.6B00149
Lin, C.-C., Ki, C. S., & Shih, H. (2015). Thiol–norbornene photoclick hydrogels for tissue engineering applications. *Journal of Applied Polymer Science, 132*(8), 41563. https://doi.org/10.1002/APP.41563
Liu, M., Zeng, X., Ma, C., Yi, H., Ali, Z., Mou, X., Li, S., Deng, Y., & He, N. (2017). Injectable hydrogels for cartilage and bone tissue engineering. *Bone Research, 5*(1), 1–20. https://doi.org/10.1038/boneres.2017.14
Lucenius, J., Valle-Delgado, J. J., Parikka, K., & Österberg, M. (2019). Understanding hemicellulose-cellulose interactions in cellulose nanofibril-based composites. *Journal of Colloid and Interface Science, 555*, 104–114. https://doi.org/10.1016/j.jcis.2019.07.053
Malafaya, P. B., Silva, G. A., & Reis, R. L. (2007). Natural–origin polymers as carriers and scaffolds for biomolecules and cell delivery in tissue engineering applications. *Advanced Drug Delivery Reviews, 59*(4–5), 207–233. https://doi.org/10.1016/J.ADDR.2007.03.012
Markstedt, K., Xu, W., Liu, J., Xu, C., & Gatenholm, P. (2017). Synthesis of tunable hydrogels based on O-acetyl-galactoglucomannans from spruce. *Carbohydrate Polymers, 157*, 1349–1357. https://doi.org/10.1016/j.carbpol.2016.11.009
Münster, L., Vícha, J., Klofáč, J., Masař, M., Kucharczyk, P., & Kuřitka, I. (2017). Stability and aging of solubilized dialdehyde cellulose. *Cellulose, 24*(7), 2753–2766. https://doi.org/10.1007/S10570-017-1314-X
Nawaz, H. A., Schröck, K., Schmid, M., Krieghoff, J., Maqsood, I., Kascholke, C., Kohn-Polster, C., Schulz-Siegmund, M., & Hacker, M. C. (2021). Injectable oligomer-cross-linked gelatine hydrogelsviaanhydride-amine-conjugation. *Journal of Materials Chemistry B, 9*(9), 2295–2307. https://doi.org/10.1039/d0tb02861d
Nemir, S., & West, J. L. (2010). Synthetic materials in the study of cell response to substrate rigidity. *Annals of Biomedical Engineering, 38*(1), 2–20. https://doi.org/10.1007/s10439-009-9811-1
Ning, Z., Tan, B., Chen, B., Lau, D. S. A., Wong, T. M., Sun, T., Peng, S., Li, Z., & Lu, W. W. (2019). Precisely controlled delivery of abaloparatide through injectable hydrogel to promote bone regeneration. *Macromolecular Bioscience, 19*(6), 1900020. https://doi.org/10.1002/mabi.201900020
Nypelö, T., Berke, B., Spirk, S., & Sirviö, J. A. (2021). Review: Periodate oxidation of wood polysaccharides—Modulation of hierarchies. *Carbohydrate Polymers, 252*, Article 117105. https://doi.org/10.1016/J.CARBPOL.2020.117105
Park, H., Woo, E. K., & Lee, K. Y. (2014). Ionically cross-linkable hyaluronate-based hydrogels for injectable cell delivery. *Journal of Controlled Release, 196*, 146–153. https://doi.org/10.1016/j.jconrel.2014.10.008
Qi, C., Liu, J., Jin, Y., Xu, L., Wang, G., Wang, Z., & Wang, L. (2018). Photo-crosslinkable, injectable sericin hydrogel as 3D biomimetic extracellular matrix for minimally invasive repairing cartilage. *Biomaterials, 163*, 89–104. https://doi.org/10.1016/j.biomaterials.2018.02.016
Ruan, C., Strømme, M., & Lindh, J. (2016). A green and simple method for preparation of an efficient palladium adsorbent based on cysteine functionalized 2,3-dialdehyde cellulose. *Cellulose, 23*(4), 2627–2638. https://doi.org/10.1007/s10570-016-0976-0
Sampath, U. G. T. M., Ching, Y. C., Chuah, C. H., Singh, R., & Lin, P. C. (2017). Preparation and characterization of nanocellulose reinforced semi-interpenetrating polymer network of chitosan hydrogel. *Cellulose, 24*(5), 2215–2228. https://doi.org/10.1007/s10570-017-1251-8
Seiffert, S. (2017a). Scattering perspectives on nanostructural inhomogeneity in polymer network gels. *Progress in Polymer Science, 66*, 1–21. https://doi.org/10.1016/J.PROGPOLYMSCI.2016.12.011
Seiffert, S. (2017b). Origin of nanostructural inhomogeneity in polymer-network gels. *Polymer Chemistry, 8*(31), 4472–4487. https://doi.org/10.1039/C7PY01035D
Shen, Y., Tang, H., Huang, X., Hang, R., Zhang, X., Wang, Y., & Yao, X. (2020). DLP printing photocurable chitosan to build bio-constructs for tissue engineering. *Carbohydrate Polymers, 235*, Article 115970. https://doi.org/10.1016/j.carbpol.2020.115970
Sun, B., Hou, Q., Liu, Z., & Ni, Y. (2015). Sodium periodate oxidation of cellulose nanocrystal and its application as a paper wet strength additive. *Cellulose, 22*(2), 1135–1146. https://doi.org/10.1007/s10570-015-0575-5
Sundberg, A., Sundberg, K., Lillandt, C., & Holmbom, B. (1996). Determination of hemicelluloses and pectins in wood and pulp fibres by acid methanolysis and gas chromatography. *Nordic Pulp and Paper Research Journal, 11*(4), 216–219. https://doi.org/10.3183/npprj-1996-11-04-p216-219
Sunyer, R., Jin, A. J., Nossal, R., & Sackett, D. L. (2012). Fabrication of hydrogels with steep stiffness gradients for studying cell mechanical response. *PLOS ONE, 7*(10), Article e46107. https://doi.org/10.1371/JOURNAL.PONE.0046107
Thomas, B., Raj, M. C., B, A. K., H, R. M., Joy, J., Moores, A., Drisko, G. L., & Sanchez, C. (2018). Nanocellulose, a versatile green platform: From biosources to materials and their applications. *Chemical Reviews, 118*(24), 11575–11625. https://doi.org/10.1021/ACS.CHEMREV.7B00627
Wang, S., Chi, J., Jiang, Z., Hu, H., Yang, C., Liu, W., & Han, B. (2021). A self-healing and injectable hydrogel based on water-soluble chitosan and hyaluronic acid for vitreous

substitute. *Carbohydrate Polymers, 256*, Article 117519. https://doi.org/10.1016/j.carbpol.2020.117519

Wang, X., Cheng, F., Liu, J., Smått, J. H., Gepperth, D., Lastusaari, M., Xu, C., & Hupa, L. (2016). Biocomposites of copper-containing mesoporous bioactive glass and nanofibrillated cellulose: Biocompatibility and angiogenic promotion in chronic wound healing application. *Acta Biomaterialia, 46*, 286–298. https://doi.org/10.1016/j.actbio.2016.09.021

Weng, L., Boda, S. K., Teusink, M. J., Shuler, F. D., Li, X., & Xie, J. (2017). Binary doping of strontium and copper enhancing osteogenesis and angiogenesis of bioactive glass nanofibers while suppressing osteoclast activity. *ACS Applied Materials and Interfaces, 9*(29), 24484–24496. https://doi.org/10.1021/acsami.7b06521

Wu, J., Li, G., Ye, T., Lu, G., Li, R., Deng, L., Wang, L., Cai, M., & Cui, W. (2020). Stem cell-laden injectable hydrogel microspheres for cancellous bone regeneration. *Chemical Engineering Journal, 393*, Article 124715. https://doi.org/10.1016/j.cej.2020.124715

Wu, J., Zheng, K., Huang, X., Liu, J., Liu, H., Boccaccini, A. R., Wan, Y., Guo, X., & Shao, Z. (2019). Thermally triggered injectable chitosan/silk fibroin/bioactive glass nanoparticle hydrogels for in-situ bone formation in rat calvarial bone defects. *Acta Biomaterialia, 91*, 60–71. https://doi.org/10.1016/j.actbio.2019.04.023

Xu, W., Zhang, X., Yang, P., Långvik, O., Wang, X., Zhang, Y., Cheng, F., Österberg, M., Willför, S., & Xu, C. (2019). Surface engineered biomimetic inks based on UV cross-linkable wood biopolymers for 3D printing. *ACS Applied Materials and Interfaces, 11*(13), 12389–12400. https://doi.org/10.1021/acsami.9b03442

Yang, X., Bakaic, E., Hoare, T., & Cranston, E. D. (2013). Injectable polysaccharide hydrogels reinforced with cellulose nanocrystals: Morphology, rheology, degradation, and cytotoxicity. *Biomacromolecules, 14*(12), 4447–4455. https://doi.org/10.1021/bm401364z

Ye, W., Li, H., Yu, K., Xie, C., Wang, P., Zheng, Y., Zhang, P., Xiu, J., Yang, Y., Zhang, F., He, Y., & Gao, Q. (2020). 3D printing of gelatin methacrylate-based nerve guidance conduits with multiple channels. *Materials and Design, 192*, Article 108757. https://doi.org/10.1016/j.matdes.2020.108757

Yilmaz, G., & Yagci, Y. (2020). Light-induced step-growth polymerization. *Progress in Polymer Science, 100*, Article 101178. https://doi.org/10.1016/J.PROGPOLYMSCI.2019.101178

Yu, C., Schimelman, J., Wang, P., Miller, K. L., Ma, X., You, S., Guan, J., Sun, B., Zhu, W., & Chen, S. (2020). Photopolymerizable biomaterials and light-based 3D printing strategies for biomedical applications. *Chemical Reviews, 120*(19), 10695–10743. https://doi.org/10.1021/ACS.CHEMREV.9B00810

Zhang, Y., Gao, C., Li, X., Xu, C., Zhang, Y., Sun, Z., Liu, Y., & Gao, J. (2014). Thermosensitive methyl cellulose-based injectable hydrogels for post-operation anti-adhesion. *Carbohydrate Polymers, 101*(1), 171–178. https://doi.org/10.1016/j.carbpol.2013.09.001

Zheng, K., Dai, X., Lu, M., Hüser, N., Taccardi, N., & Boccaccini, A. R. (2017). Synthesis of copper-containing bioactive glass nanoparticles using a modified Stöber method for biomedical applications. *Colloids and Surfaces B: Biointerfaces, 150*, 159–167. https://doi.org/10.1016/j.colsurfb.2016.11.016